Texture development in friction stir welds

R. W. Fonda* and K. E. Knipling

The shear textures that develop in friction stir welds are reviewed and discussed. In all the materials examined, including face centred cubic (fcc), body centred cubic (bcc) and hexagonal close-packed (hcp) materials, friction stir welding produces a predominant shear texture with the close-packed directions aligned with the shear direction (SD) and the close-packed plane normal perpendicular to both the SD and the shear plane normal. This orientation corresponds to the $B/\bar{B}$ ideal shear texture in fcc materials, the D_1 ideal shear texture in bcc materials, and the P_1 ideal shear texture in hcp titanium alloys. Titanium friction stir welds fabricated above the β transus temperature can contain evidence of ideal shear texture components from both the bcc D_1 (after transformation to the hcp phase according to the Burgers orientation relationship) and the hcp P_1 shear textures. Thus, similar shear textures develop in friction stir welds of fcc, bcc and hcp materials.

Introduction

Friction stir welding (FSW) is a relatively new, solid state joining process developed by The Welding Institute (Cambridge, UK).[1] During FSW, a rotating non-consumable tool is plunged into the workpiece, generating frictional heating between the tool and the workpiece and adiabatic heating through deformation of the surrounding material. This softens the surrounding material, enabling material flow ('stirring') around the rotating tool. As the tool is traversed along the joint line material is continually swept around the rotating tool and deposited in its wake, forming a consolidated joint between the two sides of the workpiece. Since no melting is involved, many problems normally associated with conventional welding are eliminated or reduced (e.g. porosity, solidification cracking, shrinkage and distortion). Friction stir welding was initially developed for aluminium alloys, but has since been demonstrated for copper, iron, titanium and magnesium alloys.[2]

The heat and deformation introduced by the rotating tool into the surrounding material can produce a variety of microstructures and textures. The predominant mode of deformation, particularly in regions near the tool, is simple shear, as confirmed in previous FSW studies of aluminium alloys.[3–8] It has been demonstrated that continuous dynamic recrystallisation, i.e. the concurrent processes of deformation and dynamic recovery, is generally the dominant process occurring in the weld nugget.[7,9–11] Geometric dynamic recrystallisation[6] has also been reported to contribute to the final observed microstructure, and there has also been evidence that discontinuous dynamic recrystallisation (DDRX)[10] and particle stimulated nucleation (PSN)[12] can occur during FSW. Textures reflecting the compressive and shear deformation introduced by the tool shoulder may be observed, primarily near the top surface where the influence of the shoulder is most pronounced. Throughout most of the friction stir weld, however, the shear induced deformation from the rotating tool would be expected to generate textures that are predominantly shear in nature. By comparison, new grain orientations introduced through DDRX or PSN would result in a more random texture.
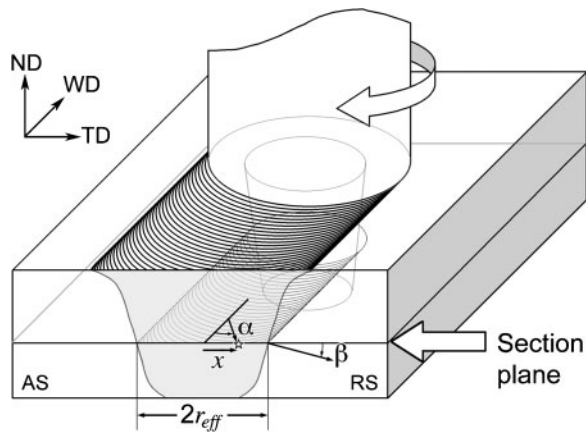
Geometric considerations

A FSW tool generally consists of a shoulder and a pin, as shown schematically in Fig. 1. Specific tool geometries can vary widely because of differences in shoulder diameter, pin geometry (straight versus tapered), threads and/or flats on the pin and/or shoulder, and other features.[2] The combined influences of the shoulder and pin produce a weld nugget that, in transverse cross section, is generally basin shaped, widening toward the top of the weld.

The predominantly shear deformation introduced by the rotating tool varies as a function of position across the weld. At each point around the tool, the shear direction (SD) is tangential to the tool surface and the shear plane normal (SPN) is perpendicular to that surface, which aligns the rotation direction (RD) with the inclined vertical surface of the tool. Because the shear deformation field reflects contributions from both the tool pin surface and the shoulder, these shear orientations are actually aligned with the effective tool surface, resulting from the combined influences of the pin and shoulder and can be estimated from the inclination of the trace of the weld nugget boundary in a transverse cross-section of the weld (Fig. 1). During the welding process, material is deposited behind the tool along this effective tool surface, which is roughly

Naval Research Laboratory, Washington DC 20375, USA

*Corresponding author, email fonda@anvil.nrl.navy.mil

Report Documentation Page		

1. REPORT DATE **DEC 2010**	2. REPORT TYPE	3. DATES COVERED **00-00-2010 to 00-00-2010**
4. TITLE AND SUBTITLE **Texture development in friction stir welds**		5a. CONTRACT NUMBER
		5b. GRANT NUMBER
		5c. PROGRAM ELEMENT NUMBER
6. AUTHOR(S)		5d. PROJECT NUMBER
		5e. TASK NUMBER
		5f. WORK UNIT NUMBER
7. PERFORMING ORGANIZATION NAME(S) AND ADDRESS(ES) **Naval Research Laboratory,Washington,DC,20375**		8. PERFORMING ORGANIZATION REPORT NUMBER
9. SPONSORING/MONITORING AGENCY NAME(S) AND ADDRESS(ES)		10. SPONSOR/MONITOR'S ACRONYM(S)
		11. SPONSOR/MONITOR'S REPORT NUMBER(S)

12. DISTRIBUTION/AVAILABILITY STATEMENT
Approved for public release; distribution unlimited

13. SUPPLEMENTARY NOTES

14. ABSTRACT

15. SUBJECT TERMS

16. SECURITY CLASSIFICATION OF:			17. LIMITATION OF ABSTRACT	18. NUMBER OF PAGES	19a. NAME OF RESPONSIBLE PERSON
a. REPORT **unclassified**	b. ABSTRACT **unclassified**	c. THIS PAGE **unclassified**	**Same as Report (SAR)**	**7**	

1 Schematic of friction stir welding process. The angular deviation α of the shear direction from the weld direction (WD) can be calculated from the effective radius of the weld nugget at the section plane (r_{eff}) and the distance from the weld centre x. The angle β indicates the inclination of the effective tool surface

2 Schematic illustrating experimentally measured crystallographic orientations and their rotation into shear frame of reference using rotations of α and β

semicircular in plan view. The SD deviates from the welding direction (WD) as a function of position across the weld by the angle α, which is defined by

$$\alpha = \sin^{-1}\left(\frac{x}{r_{eff}}\right) \qquad (1)$$

where x is the distance along the transverse direction (TD) from the weld centre and r_{eff} is the weld nugget radius (or half-width) at that depth. This equation demonstrates how SD varies in orientation from being parallel to WD at the advancing edge of the weld nugget, to aligning opposite TD at the centre of the weld, and finally to aligning opposite WD at the retreating side of the weld nugget.

The SPN direction is perpendicular to the effective tool surface, which is approximated by the shape of the weld nugget along each side of the weld in the transverse cross-section (Fig. 1). From the geometry of the tool and FSW process, it is reasonable to assume that this effective tool surface shape is maintained across the weld with (semi-)cylindrical symmetry. Thus, the SPN can be determined for each position in the weld by a rotation about SD, β, which reflects the inclination of the effective tool surface at that depth in the weld. The orientation of each location in the weld can then be represented as pole figures in the shear deformation frame of reference by aligning SD horizontally and SPN vertically as shown in Fig. 2.

In order to compare the experimentally observed textures to the textures reported in the literature, it is essential in many cases to establish and track the appropriate sense of shear. The shear in the deposited weld is determined by the tool rotation direction and WD, as indicated in Fig. 1. After the appropriate rotations to align the SD and SPN as described above, the observed shear texture can be compared to previous reports of shear textures to identify the shear components present in the weld. It is critical to establish these rotations accurately, since the shear texture components differ only in orientation and can be readily misidentified if the correct rotations are not applied. It is best to correlate the textures from at least two disparate regions of the weld that have been rotated into the shear
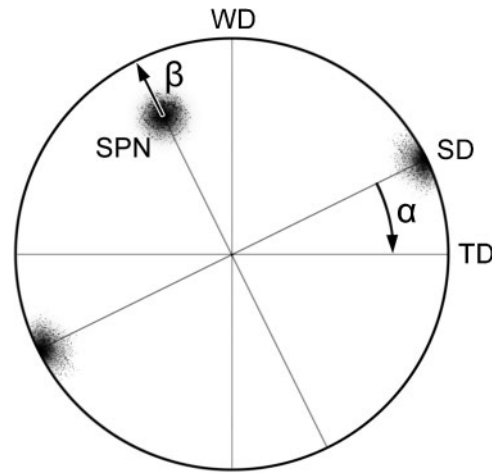
reference frame using consistent geometric rotations to ensure that those rotations produce a similar final texture. Textures reported in the literature are often reported for a negative shear, in which the top of the deformed material is sheared towards the left. This negative shear convention will be used throughout the current paper.

Textures observed in fcc materials

The ideal shear textures that can develop in fcc materials generally follow from continuous lattice rotations favouring alignment of the {111} slip plane with the shear plane and/or the $\langle 110 \rangle$ slip direction with the SD, leading to development of the A and B fibre orientations respectively.[13–16] The ideal shear textures for fcc materials are identified in Table 1 and shown in Fig. 3.

Research on the textures produced during FSW of fcc metals has primarily focused on aluminium alloys, which exhibit a predominant {112} $\langle 110 \rangle$ texture,[4–6,11,21,22] corresponding to the B and $\bar{B}$ components of the ideal shear texture. These shear textures lie on the B fibre with a close-packed $\langle 110 \rangle$ direction aligned with the SD and a close-packed {111} plane aligned with the shear rotation direction, which lies perpendicular to both the SD and SPN. This texture has also been observed in high temperature torsion[14,23] and equal channel angular extrusion[24,25] of aluminium alloys. The dominance of the $B/\bar{B}$ texture in aluminium friction stir welds indicates a large amount of shear strain introduced into that material during deposition,[23] as would be expected from the FSW process.

Periodic variations in texture have also been observed along the length of the deposited weld,[4–6,26,27] and are believed to be related to the 'onion ring' structure observed in these welds. This variation was determined to correspond to a textural variation between the $B/\bar{B}$ and the C components of the fcc ideal shear texture.[21] Like the B and $\bar{B}$ components, the C component also aligns $\langle 110 \rangle$ with the SD, but {001} is aligned with the shear plane. The C component is more prevalent at smaller shear strains than the B and $\bar{B}$ components,[23] indicating that the material deposited behind the tool during FSW was not subjected to a uniform deformation history. Furthermore, more recent observations of alternating B and $\bar{B}$ shear components along the
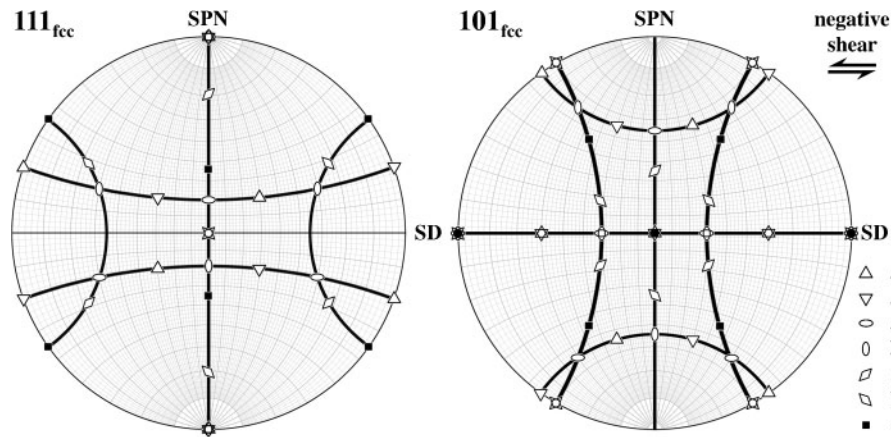
3 Pole figures showing important ideal orientations associated with simple shear deformation of fcc materials

deposited weld[28,29] indicate that material may be subject to an alternating sense of the shear deformation during the FSW process.

While the $B/\bar{B}$ shear texture is the predominant one observed, other textures have also been reported in aluminium alloys. In a recent study of texture evolution during FSW of thin 6016 aluminium sheets, Suhuddin *et al.*[22] reported that a $B/\bar{B}$ shear texture observed adjacent to the tool exit hole evolved across the width of the shoulder to a {100} ⟨001⟩ cube texture, which was maintained throughout the rest of the weld. Alternatively, McNelley *et al.*[12] demonstrated that aluminium alloys containing larger volume fractions of dispersed particles may be susceptible to PSN of new grains, which would lead to a random texture in the deposited weld nugget.

In fcc metals, stacking fault energy (SFE) has a strong influence on the operating recovery and recrystallisation processes, and hence on the resulting textures observed. The relatively large SFE for aluminium alloys results in the development and persistence of deformation textures that are observed throughout the deposited weld, as described above. In lower SFE materials such as copper alloys and austenitic stainless steels, static recrystallisation can produce thermally stable grains having different orientations from those developed during the stirring process. Saukkonen *et al.*[30] reported that a weak ⟨101⟩ fibre texture was developed by DDRX during FSW of copper. Oh-Ishi *et al.*[31] studied the textures produced during FSW of a Ni–Al bronze and found that while *A*- and *B*-type fcc ideal shear texture components developed just outside of the stir zone, the stir zone itself exhibited

Table 1 Ideal crystallographic orientations of fcc [Toth-1989-2197, Li-2005-66], bcc [Baczynski-1996-4273, Li-2005-66], and hcp [Beausir-2007-2695, Li-2008-1031] simple shear deformation textures with Euler angles (Bunge's notation) of these orientations (only $\varphi_2 = 0°$ and $\varphi_2 = 45°$ sections shown for fcc and bcc)

| | Texture | Description | Euler angles (°) | | |
			φ_1	Φ	φ_2
fcc	A₁*	{111}⟨$\bar{1}1\bar{2}$⟩	35·3/215·3	45	0
			125·3/305·3	90	45
	A₂*	{111}⟨11$\bar{2}$⟩	144·7/324·7	45	0
			54·7/234·7	90	45
	A	{1$\bar{1}$1} ⟨110⟩	0	35·3	45
	$\bar{A}$	{1$\bar{1}$1} ⟨$\bar{1}\bar{1}$0⟩	180	35·3	45
	B	{1$\bar{1}$2} ⟨110⟩	0/120/240	54·7	45
	$\bar{B}$	{$\bar{1}$1$\bar{2}$} ⟨$\bar{1}\bar{1}$0⟩	60/180/300	54·7	45
	C	{001} ⟨110⟩	90/270	45	0
			0/180	90	45
bcc	D₁	{$\bar{1}\bar{1}$2} ⟨111⟩	54·7/234·7	45	0
			144·7/324·7	90	45
	D₂	{11$\bar{2}$} ⟨111⟩	125·3/305·3	45	0
			35·3/215·3	90	45
	E	{110} ⟨1$\bar{1}$1⟩	90	35·3	45
	$\bar{E}$	{$\bar{1}\bar{1}$0} ⟨1$\bar{1}$1⟩	270	35·3	45
	J	{110} ⟨1$\bar{1}\bar{2}$⟩	90/210/330	54·7	45
	$\bar{J}$	{$\bar{1}\bar{1}$0} ⟨$\bar{1}$1$\bar{2}$⟩	30/150/270	54·7	45
	F	{110} ⟨ 001⟩	0/180	45	0
			90/270	90	45
hcp	B-fiber	{0001} ⟨*uvtw*⟩	0	90	0–60
	P-fiber	{*hkil*} ⟨11$\bar{2}$0⟩	0	0–90	0
	P₁	{1$\bar{1}$00} ⟨11$\bar{2}$0⟩	0	0	0
	Y-fiber	[0001] ±30° from RD towards SPN	0	30	30–60
	C₁-fiber	[0001] −30° from SD towards SPN	60	90	0–60
	C₂-fiber	[0001] 30° from SD towards SPN	120	90	0–60
	h5-fiber	[0001] −5° from SD towards SPN	85	90	0–60
	h6-fiber	[0001] 50° from SD towards SPN	140	90	0–60
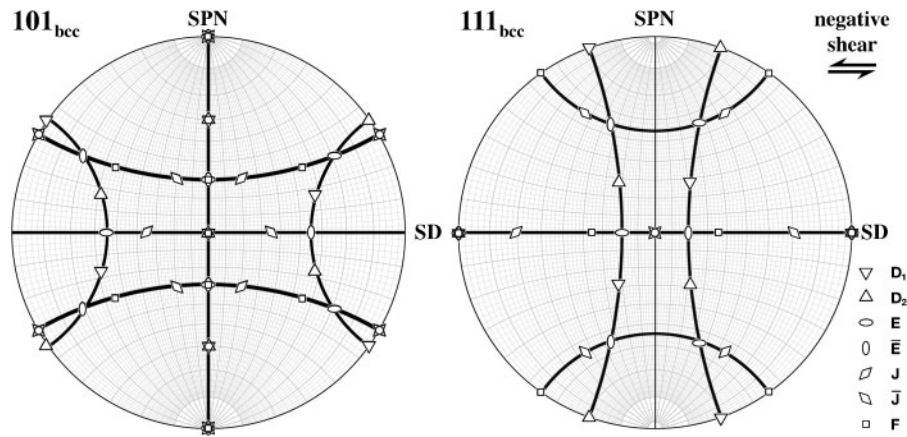
4 Pole figures showing important ideal orientations associated with simple shear deformation of bcc materials (after Baczynski and Jonas[18] and Li *et al.*[17])

a random texture which was attributed to PSN. Sato *et al.*[32] investigated the recrystallisation phenomenon during FSW of a 304 L austenitic stainless steel, and reported that the stir zone texture evolved from a {111} ⟨211⟩ texture into a {001} ⟨100⟩ cube texture, which was a result of static recrystallisation. The {001} ⟨100⟩ cube texture has also been observed in the austenitic phase of a duplex stainless steel during FSW.[33] At this time, the only models to examine the evolution of textures during FSW focused on 304 L austenitic stainless steel[34–36] and predict the formation of *A* and *B* fibres of the simple shear textures around the tool. Thus, for these lower stacking fault materials, the FSW process appears to be much more likely to generate fibre textures and other less well developed textures than was observed after FSW of aluminium alloys.

Textures observed in bcc materials

Baczynski and Jonas[18] provided the first complete analysis of the textures that develop during torsion of bcc iron alloys. They identified four ideal orientations, named *D*, *E*, *F* and *J*, and described their locations along two partial fibres: {110} ⟨uvw⟩ and {hkl} ⟨111⟩. The former contains the *F*, *J*, *J̄*, *E* and *Ē* ideal components and the latter includes the D_1, D_2, *E* and *Ē* components. These fibres are analogous to those for fcc materials, but the *hkl* and *uvw* indices are switched to reflect the interchanged close-packed directions and close-packed planes between the fcc and bcc crystal structures. More recently, Li *et al.*[17]

studied these simple shear textures during simulated equal channel angular extrusion of a bcc metal, revising Baczynski and Jonas' original notation of the bcc ideal shear texture orientations to emphasise the similarities between the bcc shear textures and the fcc ones. These revised bcc ideal shear orientations are provided in Table 1 and displayed in Fig. 4; Li *et al.*'s convention is used throughout this paper.

While there are several reports on the development of weld microstructures during the FSW of steel and other bcc metals,[34,37–39] those studies that focus on the crystallographic textures produced in bcc materials are relatively limited. Mironov *et al.*[39] determined the shear textures produced during friction stir processing (FSP, a similar process to FSW) of pure iron. Rotating the textures observed in three different regions of the weld transverse cross-section into the shear reference frame, these researchers observed consistent textures corresponding to a $D_1(\bar{1}\bar{1}2)[111]$ bcc ideal shear texture using the convention in Fig. 4. Reynolds *et al.*[40] studied the textures produced in a *β* titanium alloy, *β*-21S, which retains the metastable bcc structure at ambient temperatures. They found that rotating their pole figure data by ∼30° resulted in excellent agreement with the shear textures reported by Rollett and Wright[41] for bcc tantalum. The present authors later demonstrated,[42] however, that Reynolds *et al.*'s unrotated textures also matched the $D_2(11\bar{2})[111]$ bcc shear texture component in Baczynski and Jonas[18] notation, corresponding to a $D_1(\bar{1}\bar{1}2)[111]$ bcc shear texture in Li *et al.*'s[17] notation.
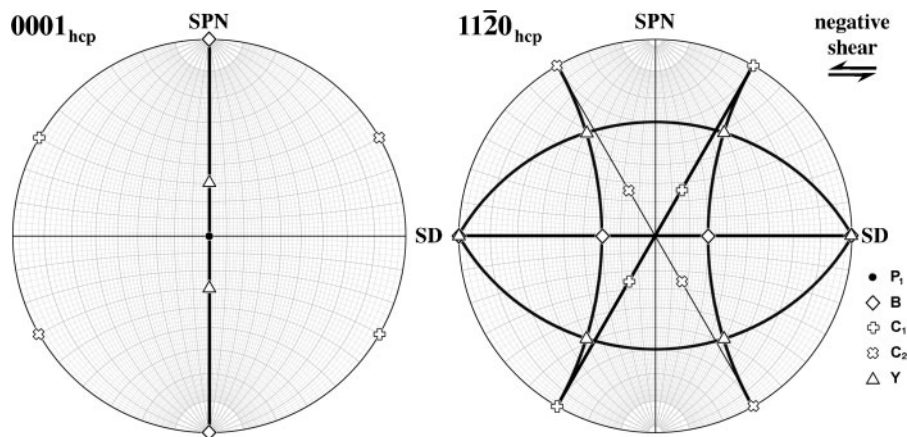
5 Pole figures showing important ideal orientations associated with simple shear deformation of hcp materials

Textures observed in hexagonal close-packed materials

Unlike fcc and bcc materials, which have multiple independent slip systems (12 and up to 48 respectively), the number of slip systems for hcp crystal structures are few, primarily limited to basal $\{0001\}$ $\langle11\bar{2}0\rangle$, prismatic $\{10\bar{1}0\}$ $\langle11\bar{2}0\rangle$, or pyramidal $\{10\bar{1}1\}$ $\langle11\bar{2}0\rangle$ slip.[43–49] The relative ease of a particular slip system depends largely upon the c/a ratio of the hcp crystal, with slip on prismatic or pyramidal planes becoming more prevalent at smaller c/a ratios. Thus the deformation mechanisms, and the resultant textures produced, are likely to vary among different hcp materials.

The first detailed analysis of hcp shear textures was by Beausir *et al.*,[19] who applied crystal plasticity theory to determine the ideal shear orientations and their persistence characteristics during simple shear of magnesium, and verified those results with the textures produced during torsion testing. The possible hcp simple shear textures consist of five fibres, named B, P, Y, C_1 and C_2, and the end orientation of the P fibre, named P_1. Beausir *et al.* demonstrated that the Y fibre is only convergent from $30° \leqslant \phi_2 \leqslant 60°$ and that only one of the C fibres is convergent. Furthermore, they indicated that the large rotation vectors around the Y and C fibres would prevent any significant intensities from developing around those fibres. A similar analysis by Li[20] additionally predicted two possible twin induced shear fibres, which were labelled $h5$ and $h6$, and determined the most stable orientations along each of these ideal shear orientation fibres. These hcp ideal shear orientations are described in Table 1 and shown in Fig. 5 (excluding $h5$ and $h6$).

Magnesium alloys

Magnesium has an axial ratio of $c/a=1·624$ (near the $1·633$ ideal) and the critical resolved shear stress for basal $\{0001\}$ slip is much smaller than that for slip on prismatic $\{10\bar{1}0\}$ or pyramidal $\{10\bar{1}1\}$ planes at ambient temperature.[44,47,50] There is considerable interest in FSW/FSP of magnesium alloys, primarily from the standpoint of of improving ductility and formability (e.g. Refs. 2, 51 and 52 and the studies cited therein). A few of these studies, however, have reported on the textures produced during FSW/FSP. The most detailed analysis is by Park *et al.*,[53] who measured the crystallographic textures produced in the weld nugget after FSW of a commercial wrought Mg–Al–Zn alloy (AZ61) using electron backscatter diffraction (EBSD). The $\{0001\}$ basal planes were consistently aligned with the pin surface, as observed from several regions within the weld nugget. Park *et al.* attributed the development of this texture to basal $\{0001\}$ $\langle11\bar{2}0\rangle$ slip, which they argued was favoured over prismatic or pyramidal slip at the high temperatures and strain rates associated with FSW. This alignment of $\{0001\}$ with the pin surface has also been observed in other magnesium FSW and FSP studies by EBSD,[54–57] X-ray diffraction[52,58,59] and neutron diffraction.[51,60,61] Mironov *et al.*[55,56] identified this observed texture as a B fibre hcp ideal shear texture, which they also attributed to $\{0001\}$ $\langle11\bar{2}0\rangle$ slip. In magnesium, the B fibre is more stable than the P fibre,[62] whereas the P fibre is prevalent in hcp titanium alloys (discussed below). This may reflect different preferences

for slip on basal, prismatic, or pyramidal planes between the two materials.

The large difference in critical resolved shear stress between basal and non-basal slip results in significant anisotropic mechanical properties of magnesium alloys, and hence the textures that develop during FSW can have strong influence on the observed mechanical properties. Several studies have reported a significant effect of stir zone texture on the tensile properties of magnesium friction stir welds.[51,60,61] Failure is typically observed at the edge of the stir zone, due to the plastic incompatibility of the orientation difference between the stir zone and the surrounding material.[60]

Titanium alloys

Unlike magnesium alloys, titanium alloys exists in two allotropic crystal forms: a low temperature α phase (hcp structure), and a high temperature β phase (bcc structure). In hcp α-titanium ($c/a=1·587$), slip occurs most readily on prismatic planes and to a lesser extent on the pyramidal or basal planes.[44,45,47,48]

Mironov *et al.*[63] studied friction stir welds in a commercial purity α titanium alloy and demonstrated that the dominant texture in the weld nugget, as measured on transverse cross-sections by EBSD, was the $P_1(1\bar{1}00)[11\bar{2}0]$ hcp ideal shear texture, which was attributed primarily to prismatic slip, with additional contributions from basal and pyramidal slip. This P_1 hcp shear texture has also been observed in friction stir welds of a near-α titanium alloy, Ti-5111.[42,64] Friction stir welds in Ti-5111 alloy also exhibit evidence of a strong $D_1(\bar{1}\bar{1}2)[111]$ bcc simple shear texture[42,64] and minor amounts of the $J/\bar{J}$ and F bcc ideal shear textures components. These bcc shear textures are modified by transformation from the high temperature bcc β phase to hcp α according to the Burgers orientation relationship (OR),[65] which maintains parallelism between the close-packed planes and close-packed directions: $\{110\}_b$ $\|$ $\{0002\}_a$ and $\langle111\rangle_b$ $\|$ $\langle11\bar{2}0\rangle_a$. The presence of these bcc shear textures indicates that the material was deformed above the β transus temperature during welding and that the observed texture was inherited directly from that high temperature bcc shear texture as the material cooled through the allotropic transformation. The D_1 bcc ideal shear texture was also observed in friction stir welds of pure iron[39] and β titanium,[40] as discussed above.

The relative strengths of the hcp P_1 and the bcc D_1 shear textures can vary with welding conditions as well as alloy composition. Fonda and Knipling[64] observed that Ti-5111 friction stir welds exhibit a stronger predominance of the high temperature bcc D_1 shear texture at fast (lower temperature) welding conditions, while there is a stronger influence of the low temperature hcp P_1 shear texture at slow (higher temperature) welding conditions. They interpreted this apparent contradiction to reflect a variation in the stirring efficiency in the wake of the tool, proposing that fast welding speeds can allow the high temperature deformation structure to be retained in the wake of the tool while slower welding speeds can enable a more efficient transfer of the stirring deformation and thereby continue to deform the deposited weld as it cools through the β transus temperature. It should be noted that while the presence of P_1 hcp shear texture components in a titanium alloy could indicate that the

shear deformation was introduced into the material at temperatures below the β transus, it could also result from an α variant selection as the material cools through the β transus in the presence of a shear deformation field, since the hcp P_1 shear texture is identical to one of the Burgers variants of the bcc D_1 shear texture.

Titanium alloys that retain the high temperature β phase at room temperature allow for a direct measure of the bcc deformation texture. The study by Reynolds *et al.*[40] on a β titanium alloy, β-21S, was discussed above. Other FSW/FSP studies have focused on $\alpha + \beta$ alloys, and Ti–6Al–4V in particular.[66–73] Mironov *et al.*[71] measured the texture of the retained β phase in the weld nugget of Ti–6Al–4V using EBSD, which reportedly matched that of a $\bar{J}(1\bar{1}0)[11\bar{2}]$ bcc ideal simple shear texture. The authors noted, however, that this texture was based on a limited number of measurements of the narrow β ribs in the colony α microstructure, and it was later pointed out[64] that their observed texture could also correspond well with the $D_1(\bar{1}\bar{1}2)[111]$ bcc ideal shear texture.

Pilchak *et al.*[73] recently studied the effects of welding parameters on the resulting microstructure in Ti–6Al–4V friction stir welds. They calculated the texture of the high temperature β phase from the observed α orientations using an automated reconstruction technique developed by Glavicic *et al.*[74,75] and assuming the Burgers OR between the α and β phases. Pilchak *et al.* reported that the reconstructed β grains exhibited a texture with $\langle 111 \rangle$ aligned with the SD, corresponding to the E and $\bar{E}$ bcc ideal shear texture components. However, the authors neglected the tilt of the effective tool surface, β, in their analysis. Rotating their data by 30° to account for this angle β brings it into coincidence with the D_1 shear texture, as has been observed in other titanium friction stir welds.

Summary

Friction stir welding is a novel joining technique that utilises a rotating tool to heat and 'stir' together two metal pieces. The predominant deformation mode in the weld nugget close to the tool is simple shear, and the crystallographic textures observed in these regions generally correspond to ideal simple shear textures. This paper reviews the ideal simple shear textures that develop in fcc, bcc and hcp materials and discusses recent studies in the literature that report these textures in FSW studies of aluminium, iron, titanium and magnesium alloys. Similar shear textures develop for most of these materials, with the close-packed directions aligned with the SD and the close-packed plane normal perpendicular to both the SD and the SPN. This orientation corresponds to the $B/\bar{B}$ ideal shear texture in fcc materials, the D_1 ideal shear texture in bcc materials, and the P_1 ideal shear texture in hcp titanium alloys. Titanium friction stir welds fabricated above the β transus temperature also exhibit D_1 bcc ideal shear texture components (which transform to the hcp phase according to the Burgers OR during cooling) in addition to the hcp P_1 shear textures. In hcp magnesium alloys, however, the close-packed {0001} basal planes are aligned with shear plane, resulting in a B fibre texture. This is perpendicular to the P_1 texture observed for α titanium, and may be reflective of differences in preferred slip systems of the two materials.

References

1. W. M. Thomas, E. D. Nicholas, J. C. Needham, M. G. Murch, P. Temple-Smith and C. J. Dawes: GB Patent Application no. 9,125,978·8, 1991; US Patent no. 5,460,317, 1995.
2. R. S. Mishra and Z. Y. Ma: *Mater. Sci. Eng. R*, 2005, **R50**, (1–2), 1–78.
3. Y. S. Sato, H. Kokawa, K. Ikeda, M. Enomoto, S. Jogan and T. Hashimoto: *Metall. Mater. Trans. A*, 2001, **32A**, (4), 941–948.
4. D. P. Field, T. W. Nelson, Y. Hovanski and K. V. Jata: *Metall. Mater. Trans. A*, 2001, **32A**, (11), 2869–2877.
5. R. W. Fonda, J. F. Bingert and K. J. Colligan: *Scr. Mater.*, 2004, **51**, (3), 243–248.
6. P. B. Prangnell and C. P. Heason: *Acta Mater.*, 2005, **53**, (11), 3179–3192.
7. R. W. Fonda, J. A. Wert, A. P. Reynolds and W. Tang: *Sci. Technol. Weld. Join.*, 2007, **12**, (4), 304–310.
8. R. W. Fonda, K. E. Knipling and J. F. Bingert: *Scr. Mater.*, 2008, **58**, (5), 343–348.
9. J. Q. Su, T. W. Nelson, R. Mishra and M. Mahoney: *Acta Mater.*, 2003, **51**, (3), 713–729.
10. J. Q. Su, T. W. Nelson and C. J. Sterling: *Mater. Sci. Eng. A*, 2005, **A405**, (1–2), 277–286.
11. R. W. Fonda and J. F. Bingert: *Metall. Mater. Trans. A*, 2006, **37A**, (12), 3593–3604.
12. T. R. McNelley, S. Swaminathan and J. Q. Su: *Scr. Mater.*, 2008, **58**, (5), 349–354.
13. G. R. Canova, U. F. Kocks and J. J. Jonas: *Acta Metall.*, 1984, **32**, (2), 211–226.
14. F. Montheillet, M. Cohen and J. J. Jonas: *Acta Metall.*, 1984, **32**, (11), 2077–2089.
15. F. Montheillet, P. Gilormini and J. J. Jonas: *Acta Metall.*, 1985, **33**, (4), 705–717.
16. L. S. Toth, K. W. Neale and J. J. Jonas: *Acta Metall.*, 1989, **37**, (8), 2197–2210.
17. S. Li, I. J. Beyerlein and M. A. M. Bourke: *Mater. Sci. Eng. A*, 2005, **A394**, (1–2), 66–77.
18. J. Baczynski and J. Jonas: *Acta Mater.*, 1996, **44**, (11), 4273–4288.
19. B. Beausir, L. S. Toth and K. W. Neale: *Acta Mater.*, 2007, 55, (8), 2695–2705.
20. S. Li: *Acta Mater.*, 2008, **56**, (5), 1031–1043.
21. R. W. Fonda and J. F. Bingert: *Scr. Mater.*, 2007, **57**, (11), 1052–1055.
22. U. F. H. R. Suhuddin, S. Mironov, Y. S. Sato and H. Kokawa: *Mater. Sci. Eng. A*, 2010, **A527**, (7–8), 1962–1969.
23. T. Pettersen and E. Nes: *Metall. Mater. Trans. A*, 2003, **34A**, (12), 2727–2736.
24. A. Gholinia, P. Bate and P. Prangnell: *Acta Mater.*, 2002, **50**, (8), 2121–2136.
25. S. Vogel, D. Alexander, I. Beyerlein, M. Bourke, D. Brown, B. Clausen, C. Tome, R. V. Dreele, C. Xu and T. Langdon: *Mater. Sci. Forum*, 2003, **426–432**, 2661–2666.
26. J. A. Schneider and A. C. Nunes: *Metall. Mater. Trans. B*, 2004, **35B**, (4), 777–783.
27. J. Pouchou, D. Boivin, Y. Renollet and C. Gallais: *Microchim. Acta*, 2004, **145**, (1–4), 171–176.
28. M. M. Z. Ahmed, B. P. Wynne, W. M. Rainforth and P. L. Threadgill: *Scr. Mater.*, 2008, **59**, (5), 507–510.
29. R. W. Fonda, A. P. Reynolds, C. R. Feng, K. E. Knipling and D. J. Rowenhorst: Proceedings of 'Thermec 2011' 2011, Trans Tech Publications Ltd, Stafa-Zurich, Switzerland.
30. T. Saukkonen, K. Savolainen, J. Mononen and H. Hänninen: Proc. 15th Int. Conf. on 'Textures of materials (ICOTOM 15)', (ed. A. D. Rollett), Hoboken, NJ, 53–60; 2008, NJ, John Wiley & Sons.
31. K. Oh-Ishi, A. P. Zhilyaev and T. R. McNelley: *Metall. Mater. Trans. A*, 2006, **37A**, (7), 2239–2251.
32. Y. S. Sato, T. W. Nelson and C. J. Sterling: *Acta Mater.*, 2005, **53**, (3), 637–645.
33. T. Saeid, A. Abdollah-Zadeh, T. Shibayanagi, K. Ikeuchi and H. Assadi: *Mater. Sci. Eng. A*, 2010, **A527**, (24–25), 6484–6488.
34. J. Cho, D. Boyce and P. Dawson: *Mater. Sci. Eng. A*, 2005, **A398**, (1–2), 146–163.
35. J. Cho and P. Dawson: *Metall. Mater. Trans. A*, 2006, **37A**, (4), 1147–1164.
36. J.-H. Cho and P. R. Dawson: *J. Eng. Mater.*, 2008, **130**, (1), 011007.
37. Y. S. Sato, T. W. Nelson, C. J. Sterling, R. J. Steel and C. O. Pettersson: *Mater. Sci. Eng. A*, 2005, **A397**, (1–2), 376–384.

38. Y. S. Sato, S. H. C. Park, A. Matsunaga, A. Honda and H. Kokawa: *J. Mater. Sci.*, 2005, **40**, (3), 637–642.
39. S. Mironov, Y. S. Sato and H. Kokawa: *Acta Mater.*, 2008, **56**, (11), 2602–2614.
40. A. P. Reynolds, E. Hood and W. Tang: *Scr. Mater.*, 2005, **52**, (6), 491–494.
41. A. D. Rollett and S. I. Wright: 'Texture and Anisotropy', (ed. U. F. Kocks *et al*), 202; 1998, Cambridge, Cambridge University Press.
42. K. E. Knipling and R. W. Fonda: *Scr. Mater.*, 2009, **60**, (12), 1097–1100.
43. A. T. Churchman: *Proc. R. Soc. Lond. A*, 1954, **226A**, (1165), 216–226.
44. P. G. Partridge: *Metall. Rev.*, 1967, **12**, 169–194.
45. M. H. Yoo: *Metall. Trans. A*, 1981, **12A**, (3), 409–418.
46. I. P. Jones and W. B. Hutchinson: *Acta Metall.*, 1981, **29**, (6), 951–968.
47. H. Numakura and M. Koiwa: *Metall. Sci. Technol.*, 1998, **16**, (1–2), 4–19.
48. G. Lutjering and J. C. Williams: 'Titanium'; 2003, New York, Springer.
49. W. B. Hutchinson and M. R. Barnett: *Scr. Mater.*, 2010, **63**, (7), 737–740.
50. A. Couret and D. Caillard: *Acta Metall.*, 1985, **33**, (8), 1447–1454.
51. W. Woo, H. Choo, M. B. Prime, Z. Feng and B. Clausen: *Acta Mater.*, 2008, **56**, (8), 1701–1711.
52. J. Yang, B. L. Xiao, D. Wang and Z. Y. Ma: *Mater. Sci. Eng. A*, 2010, **A527**, (3), 708–714.
53. S. H. C. Park, Y. S. Sato and H. Kokawa: *Metall. Mater. Trans. A*, 2003, **34A**, (4), 987–994.
54. U. F. H. R. Suhuddin, S. Mironov, Y. S. Sato, H. Kokawa and C. W. Lee: *Acta Mater.*, 2009, **57**, (18), 5406–5418.
55. S. Mironov, Y. Motohashi, R. Kaibyshev, H. Somekawa, T. Mukai and K. Tsuzaki: *Mater. Trans.*, 2009, **50**, (3), 610–617.
56. S. Mironov, Q. Yang, H. Takahashi, I. Takahashi, K. Okamoto, Y. S. Sato and H. Kokawa: *Metall. Mater. Trans. A*, 2010, **41A**, (4), 1016–1024.
57. R. L. Xin, B. Li and Q. Liu: *Mater. Sci. Forum*, 2010, **654–656**, 1195–1200.
58. C. Chang, C. Lee and J. Huang: *Scr. Mater.*, 2004, **51**, (6), 509–514.
59. Y. N. Wang, C. I. Chang, C. J. Lee, H. K. Lin and J. C. Huang: *Scr. Mater.*, 2006, **55**, (7), 637–640.
60. W. Woo, H. Choo, D. Brown, P. Liaw and Z. Feng: *Scr. Mater.*, 2006, **54**, (11), 1859–1864.
61. Z. Yu, H. Choo, Z. Feng and S. C. Vogel: *Scr. Mater.*, 2010, **63**, (11), 1112–1115.
62. I. J. Beyerlein and L. S. Toth: *Prog. Mater. Sci.*, 2009, **54**, (4), 427–510.
63. S. Mironov, Y. S. Sato and H. Kokawa: *Acta Mater.*, 2009, **57**, (15), 4519–4528.
64. R. W. Fonda and K. E. Knipling: *Acta Mater.*, 2010, **58**, (19), 6452–6463.
65. W. G. Burgers: *Physica*, 1934, **1**, 561–586.
66. A. J. Ramirez and M. C. Juhas: *Mat. Sci. Forum*, 2003, **426–432**, 2999–3004.
67. A. L. Pilchak, M. C. Juhas and J. C. Williams: *Metall. Mater. Trans. A*, 2007, **38A**, (2), 401–408.
68. A. L. Pilchak, D. M. Norfleet, M. C. Juhas and J. C. Williams: *Metall. Mater. Trans. A*, 2008, **39A**, (7), 1519–1524.
69. S. Mironov, Y. Zhang, Y. Sato and H. Kokawa: *Scr. Mater.*, 2008, **59**, (5), 511–514.
70. Y. Zhang, Y. S. Sato, H. Kokawa, S. H. C. Park and S. Hirano: *Mater. Sci. Eng. A*, 2008, **A485**, (1–2), 448–455.
71. S. Mironov, Y. Zhang, Y. S. Sato and H. Kokawa: *Scr. Mater.*, 2008, **59**, (1), 27–30.
72. A. L. Pilchak and J. C. Williams: *Metall. Mater. Trans. A*, 2011, http://www.springerlink.com/content/1073-5623/42/3/, **42**, (3), 773–94.
73. A. L. Pilchak, W. Tang, H. Sahiner, A. P. Reynolds and J. C. Williams: *Metall. Mater. Trans. A*, 2010, 42A, http://www.springer-link.com/content/1073-5623/42/3/, Volume 42, Number 3, pp. 745–62.
74. M. G. Glavicic, P. A. Kobryn, T. R. Bieler and S. L. Semiatin: *Mater. Sci. Eng. A*, 2003, **A346**, (1–2), 50–59.
75. M. G. Glavicic, P. A. Kobryn, T. R. Bieler and S. L. Semiatin: *Mater. Sci. Eng. A*, 2003, **A351**, (1–2), 258–264.